

A study of the memory effects of metallic core–metal oxide shell nanocrystals by a micelle dipping technique

This article has been downloaded from IOPscience. Please scroll down to see the full text article.

2010 Nanotechnology 21 125202

(<http://iopscience.iop.org/0957-4484/21/12/125202>)

View [the table of contents for this issue](#), or go to the [journal homepage](#) for more

Download details:

IP Address: 210.123.42.187

The article was downloaded on 31/05/2013 at 13:17

Please note that [terms and conditions apply](#).

A study of the memory effects of metallic core–metal oxide shell nanocrystals by a micelle dipping technique

Chung-Jin Kim¹, Sung-Jin Choi¹, Seong-Wan Ryu¹, Sungho Kim¹,
Jae-Joon Chang², Su Hak Bae², Byeong-Hyeok Sohn² and
Yang-Kyu Choi^{1,3}

¹ Department of Electrical Engineering, College of Information Science and Technology
KAIST, 335 Gwahangno, Yuseong-gu, Daejeon 305-701, Republic of Korea

² Department of Chemistry and NANO Systems Institute, Seoul National University,
599 Gwanakro, Gwanak-gu, Seoul 151-747, Republic of Korea

E-mail: ykchoi@ee.kaist.ac.kr

Received 20 October 2009, in final form 4 January 2010

Published 2 March 2010

Online at stacks.iop.org/Nano/21/125202

Abstract

With a simple and conformal metal nanocrystal dipping of synthesized micelles, nonvolatile memory characteristics originating from a metallic cobalt (Co) core nanocrystal (NC) surrounded by a Co-oxide shell are investigated in this study. From transmission electron microscopy (TEM) and x-ray photoelectron spectroscopy (XPS), it was confirmed that Co-oxide was made by oxygen plasma for polymer oxidation and that metallic Co wrapped with a Co-oxide shell was made by hydrogen annealing in order to reduce the Co-oxide. Energy band diagrams considering the extent of the coexistent metallic Co/Co-oxide were also analyzed in terms of how they correspond to each program/erase/retention case. These cases were verified by electrically measured data. These results can provide a guideline for the design and optimization of metal NC embedded memory.

(Some figures in this article are in colour only in the electronic version)

1. Introduction

The explosive demand for solid-state Flash memory in the memory market has driven technological innovation in ultimately scaled memory. In company with this demand, it is forecast that the advent of a new memory paradigm is approaching and that the new memory will be similar to conventional Flash memory. This new memory can perhaps take the form of memory that utilizes a discrete charge trap concept using nanocrystals (NCs) [1–3] or nitride [4, 5]. Among them, NC technology has approached its product stage in the near-term by Freescale [6]. In addition to the associated scaling issue, many efforts have been made toward a simultaneous enhancement of performance and reliability. Hence, metal nanocrystal embedded memory is attractive due to the degree of design freedom presented by its workfunction

engineering [7]. Based on the attention it has received, many studies of diverse metals and derived metal oxide materials have been carried out for a discrete memory storage node [8–12]. Relevant studies, however, have concentrated solely on new materials and demonstrations of simple and typical memory characteristics. Moreover, there have been few attempts to achieve synergistic high performance through a combination of a metal and a derived metal oxide [12]. Additionally, guidelines to control the metal and metal oxide configuration have not been presented.

For ultimately scaled memory based on an ordered array template, novel approaches using diverse self-assembled materials such as a diblock copolymer with various nanostructure [13–16], protein [11, 17], DNA [18, 19], virus [20] and cluster elements [21] have been reported. It is noteworthy that easy and simple steps for the reduction of a template are advantageous. However, metal itself is susceptible to oxidation by exposure to oxygen ambient and the oxidation

³ Author to whom any correspondence should be addressed.

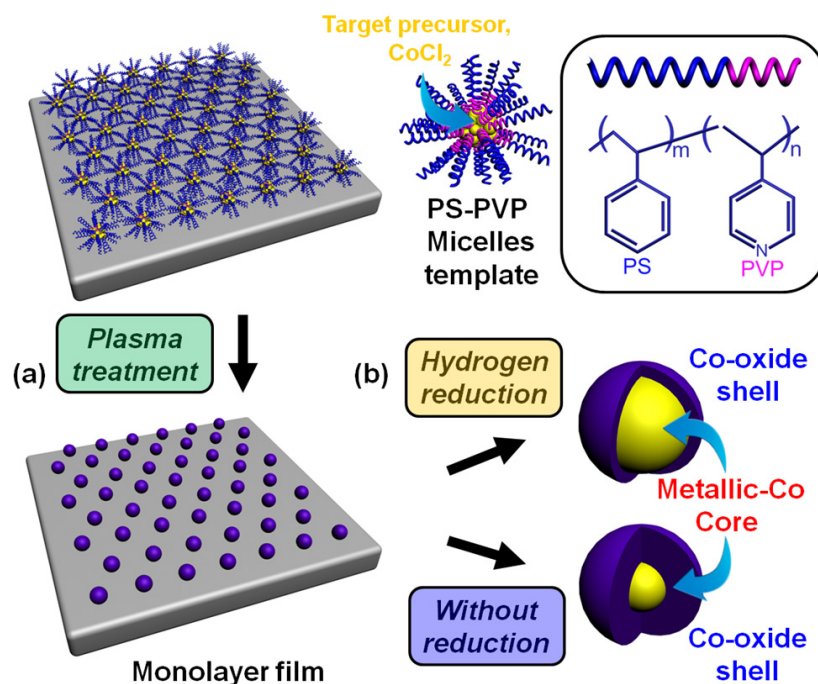


Figure 1. The schematics of the oxidation/reduction step after dip coating of Co NCs onto substrate followed by the synthesis procedure. (a) Removal of the polymeric template by oxygen plasma and the formation of Co coated arrays. (b) Configuration of Co core NCs surrounded by Co-oxide shell nanocrystals after hydrogen reduction and no reduction steps, respectively.

occurs during the removal of a polymer template. Thus, a reduction process is inevitable. In regard to this issue, it is important to study how this type of reduction step affects memory performance through a characterized comparison. Also, ultimately scaled memory has been required for the dense and uniform NC formation technique suitable for a non-planar three-dimensional (3D) structure with a multiple gate which can mitigate the short-channel-effects [22, 23].

Recently, we demonstrated a 3D vertical floating gate memory with metal NCs as the proof-of-concept of the micelle dipping technique. The resulting cobalt (Co) NCs were synthesized by means of a reversed micellar structure based on a diblock copolymer [24]. A dipping method of synthesized micelle enabled simple and uniform metal coating for 3D arrays. During the synthesis process, however, an oxygen plasma treatment was inevitably required to remove the core-shell block that served as a polymer template for the highly ordered array and hydrogen annealing was performed for the reduction of the formed metal oxide shell. In this study, the memory effects according to the core-shell fraction of the Co core NCs surrounded by a Co-oxide shell via hydrogen reduction are primarily investigated. In addition to a phenomenal memory effect, nanocrystal configurations are verified using diversified techniques such as transmission electron microscopy (TEM) and x-ray photoelectron spectroscopy (XPS), and also memory performance in terms of the program/erase/retention characteristics is carefully analyzed through simulation. A guideline is then suggested regarding the design of metal and metal oxide configurations.

2. Experiment

2.1. Process of device fabrication, procedures of micelle synthesis, and dip coating

The fabrication process of a Co NC embedded memory device using a sidewall channel has been described in previous work [22]. The procedure of micelle synthesis is as follows. Polystyrene-block-poly(4-vinyl pyridine) (PS-PVP) copolymers were purchased from Polymer Source, Inc. The average molecular weights (M_w) of PS and PVP were 32 900 and 8000 g mol⁻¹, respectively. The polydispersity index was 1.08. PS-PVP copolymers were dissolved in toluene at 75 °C for 3 h to yield a 0.5 wt% micellar solution, which was then cooled down to room temperature. A solution of PS-PVP micelles containing precursors (CoCl₂) of Co NCs was prepared by adding precursors to a micellar solution and stirring the solution for at least five days as in the upper row of figure 1. A molar ratio of the precursor to the vinyl pyridine unit was fixed at 0.5. The pattern was dipped into a solution of copolymer micelles containing precursors at a rate of 20 mm min⁻¹, subsequently pulled out of the solution at the same rate, and then dried in air. It should be noted that Co NCs are coated uniformly onto the top surface as well as the sidewall surface in the scanning electron microscopy (SEM) images [24]. In the dip coating process, conformal and monolayered NC formation was explained by the confined convective assembly at the meniscus of the air-solution interface or direct adsorption in the bulk solution [25, 26]. Therefore, the dipping method is suitable in the planar structure as well as the non-planar structure with 3D arrays and conformal metal coating possible in a large area.

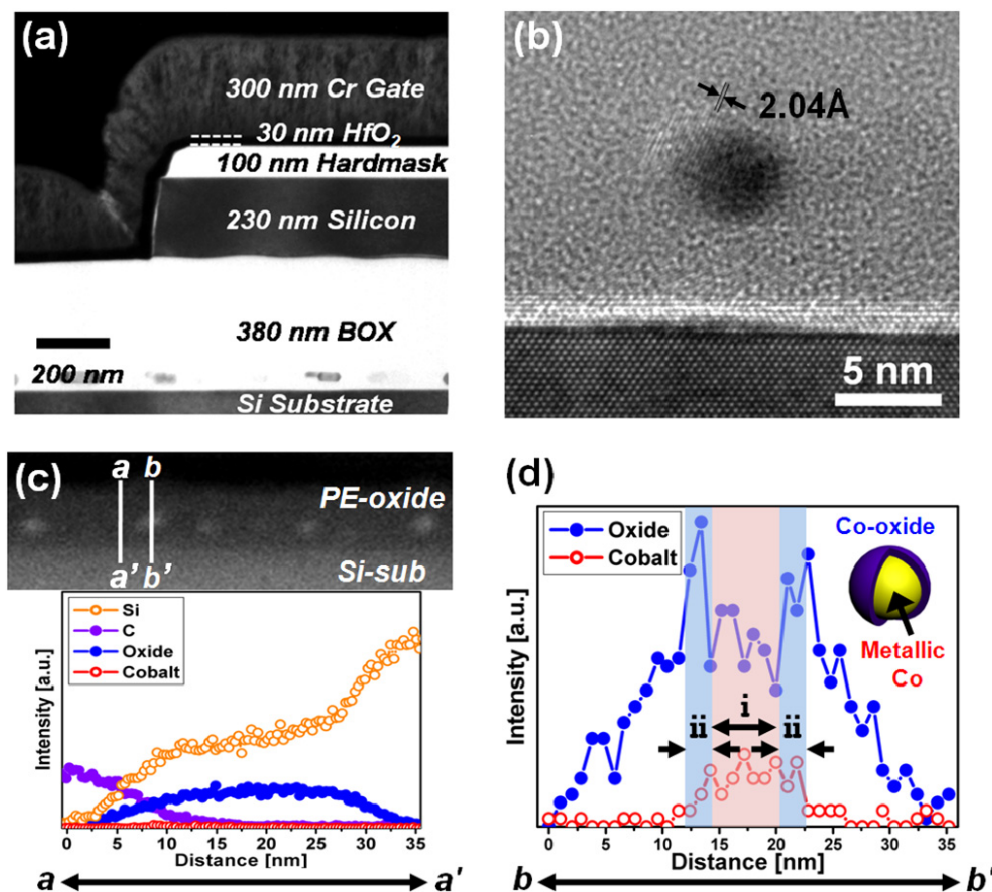


Figure 2. A cross-sectional TEM photograph of (a) the fabricated vertical floating gate device (b) the hydrogen-annealed sample. (c) An upper image of the cross-sectional HAADF-STEM photograph exhibits the location of each intensity line profile. The intensity line profile along the aa' direction of the lower graph shows no Co element. (d) The intensity line profile in the bb' direction of the inset shows the configuration of the metallic Co core/Co-oxide shell.

2.2. Oxygen plasma treatment step and hydrogen reduction step

Monolayer films of PS-PVP micelles with CoCl_2 are treated with oxygen plasma (power: 100 W, pressure: 2.0×10^{-2} Torr) for 10 min (figure 1(a)). Hydrogen annealing for reduction decreasing the oxide in the Co-oxide is performed in an ambient environment with 10% hydrogen and 90% nitrogen at 400 °C for an hour (figure 1(b)).

2.3. Characterization of nanocrystals

Nanocrystals on a 3D pattern were characterized by FEI field emission-TEM (FE-TEM, Tecnai G^2 F30). HRTEM images were obtained at 300 kV and elemental analysis with a line profile was conducted through high-angle annular dark-field scanning-TEM (HAADF-STEM). For Co nanocrystal, the lattice spacing was in agreement with the reference metallic Co pattern (JCPDS-International Center for Diffraction Data; card numbers 15-0806). XPS measurement was carried out with an ESCALAB 250 spectrometer equipped with a $\text{Al K}\alpha$ energy source.

2.4. Extraction of energy band diagram and electrical characterization

We have extracted the energy band diagram with the aid of a semiconductor simulator (Synopsys MEDICI). Based on the reported energy band information and bias conditions, tendencies in terms of the electron tunneling mechanism were investigated for each program/erase/retention mode. In the energy band simulation, the thickness of Co-oxide/metallic Co/Co-oxide as core-shell structure was set as 4 nm/2 nm/4 nm and 2 nm/6 nm/2 nm for the oxidized Co and the reduced Co, respectively (figure 1(b)). Electrical measurements were done with a semiconductor parameter analyzer (HP4156C). The drain current was measured while the gate voltage was swept with the grounded source and a drain bias of 50 mV. For a reference point of memory performance, threshold voltage (V_T) was defined from the drain voltage corresponding to the constant drain current, $10^{-7} \text{ A } \mu\text{m}^{-1}$. All measurements were performed on a probe station.

3. Results and discussion

A cross-sectional TEM image of the fabricated vertical floating gate device is shown in figure 2(a). The detailed process flow

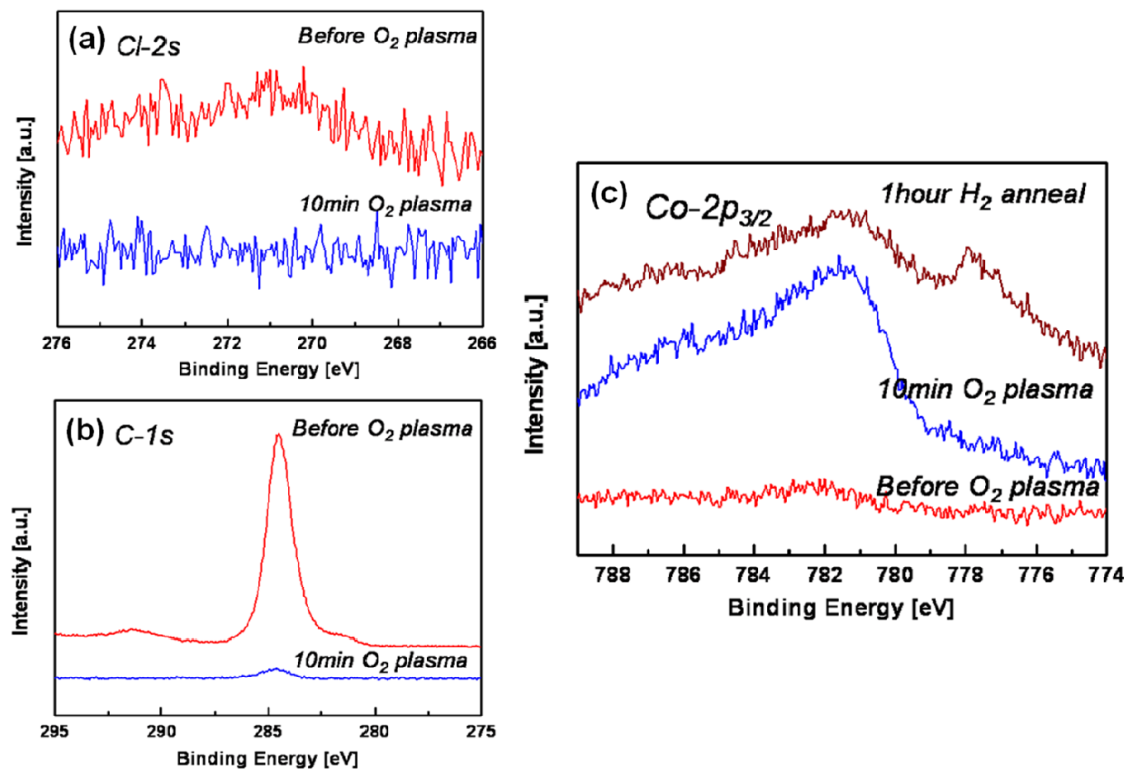


Figure 3. The XPS spectrum of Co NCs (a) before and after the oxygen plasma treatment at the Cl 2s binding energy region, (b) before and after the oxygen plasma treatment at the C 1s binding energy region, and (c) before and after the oxygen plasma treatment as well as after hydrogen annealing at the Co $2p_{3/2}$ binding energy region.

was described in the previous work [24]. Even if Co NCs are coated onto the top surface as well as the sidewall, 100 nm thick hardmask oxide plays a role as a thick gate oxide to produce a high threshold voltage (V_T) thereby making only the vertical component NCs formed on the sidewall surface serve for memory operation.

Figure 2(b) shows a TEM image of a hydrogen-annealed sample. Co NCs are encapsulated by thermally grown oxide (tunneling oxide) and a deposited plasma-enhanced (PE) oxide (control oxide). The subsequent oxygen plasma treatment step for the oxidation and hydrogen annealing step for reduction are followed. To remove the aforementioned polymer template, a coated monolayer of micelles is treated with oxygen plasma, resulting in Co-oxide NCs. Monolayer films of PS-PVP micelles with CoCl_2 are treated with oxygen plasma to leave NCs on the substrate with the removal of the copolymers. Thereafter, hydrogen annealing for reduction, i.e. decreasing the oxide in the Co-oxide, is performed. A high-resolution TEM image of the magnified Co NC image in figure 2(b) confirms that Co NC has a spherical geometry; this structure arises from the donut-shaped core-shell structure in the solution [27, 28]. The observed lattice spacing is matched with the value of $d = 2.04 \text{ \AA}$ of the metallic Co in the (111) plane (JCPDS 15-0806).

The upper image of figure 2(c) exhibits an HAADF-STEM image of conformally synthesized NCs on the tunneling oxide. The lower image of figures 2(c) and (d) indicate the intensity of each element profile along the aa' and bb' direction of the HAADF-STEM image, respectively. The intensity line

profile across the oxide layer without Co NC shows that the Co element does not exist (the high intensity of silicon and carbon elements indicate the existence of the silicon substrate and epoxy carbon during specimen preparation, respectively). The hydrogen-annealed Co NC, on the other hand, shows a 'crater-like' intensity profile along the bb' direction. The intensity of Co increases at region (i) and decreases at region (ii), whereas the intensity of the oxide is maximum at region (ii) and rapidly decreases at region (i). These results prove that a device with hydrogen annealing under the aforementioned reduction condition has the configuration of a metallic core wrapped by a metal oxide shell, with Co-oxide at the outer and metallic Co in the inner areas [12, 29]. With the assumption that the reduction process starts from the surface, it is also important to note that the Co-oxide was completely reduced to the metallic Co state by the hydrogen annealing step and then re-oxidized from the outside due to its small oxygen binding energy [30].

Figure 3 shows the XPS spectrum data after the oxygen plasma and hydrogen annealing treatment. Figures 3(a) and (b) show the chlorine (Cl) 2s and carbon (C) 1s binding energies, respectively. At the beginning stage, Co is synthesized in the form of CoCl_2 as a precursor of Co. The polymer template containing carbon is removed during the oxygen plasma treatment; Cl is also removed simultaneously. As shown in figures 3(a) and (b), the peak intensity at 271 and 284.6 eV assures the existence of Cl and C before the oxygen plasma treatment. Thus they certify complete removal of the copolymer after an oxygen plasma treatment of 10 min.

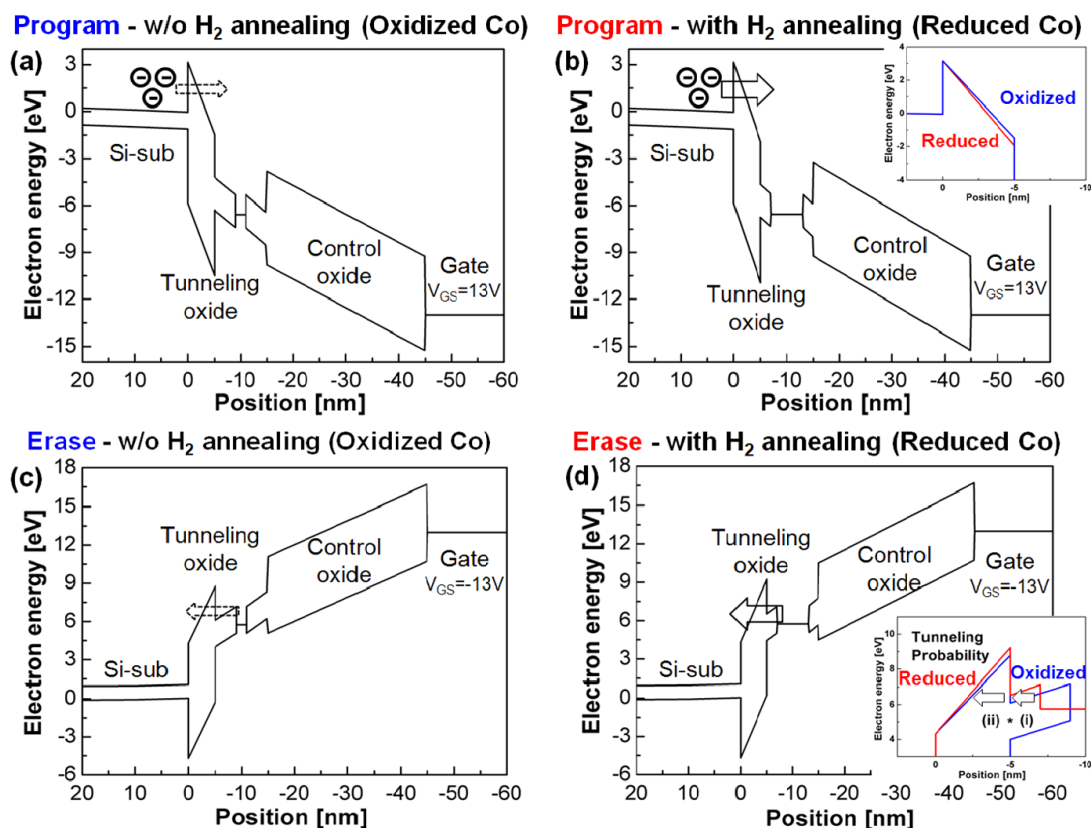


Figure 4. A schema of simulated energy band diagrams with the oxidized and reduced Co/Co-oxide composite NC embedded devices for the program (upper row—(a), (b)) and erase (lower row—(c), (d)) modes, respectively. Insets exhibit the overlapped energy band diagrams of the oxidized and reduced Co/Co-oxide composite at the tunneling oxide in the case of the program and erase modes.

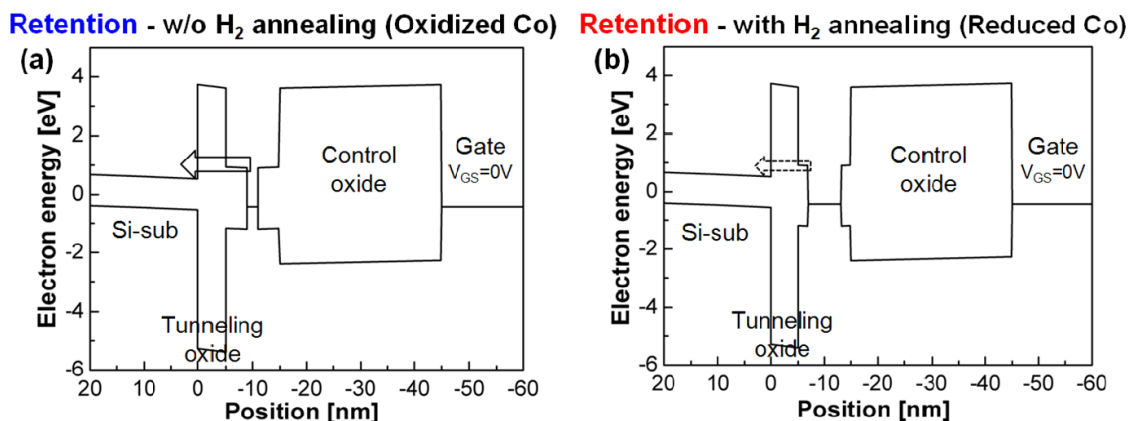


Figure 5. A schema of simulated energy band diagrams with the oxidized (a) and reduced (b) Co/Co-oxide composite NC embedded devices for the retention mode.

Figure 3(c) exhibits the Co $2p_{3/2}$ binding energy region. Before the oxygen plasma treatment, a weak peak of the micellar state is visible at 782.3 eV due to the attachment of Co to Cl and OH groups (lowest image) [31]. The oxygen treatment causes Co to become oxidized to Co_3O_4 . Its chemical state is hence ensured by the peak at 781 eV. In this step, it is worthwhile to mention that overall Co would not be oxidized to the Co-oxide state due to self-limited oxidation and it will be discussed with the energy band diagram hereafter [29]. The subsequent hydrogen annealing process

induces a reduction of this Co-oxide into metallic Co, which is identified by the peak at 778 eV. The relatively weak shoulder at 778 eV reveals that the reduced metallic Co state formed by the hydrogen annealing step is re-oxidized under ambient conditions.

Figures 4 and 5 show simulated energy band diagrams with the aid of MEDICI [32] for oxidized and reduced Co/Co-oxide composite NC embedded devices to analyze their program, erase, and retention operations, respectively. Co-oxide (Co_3O_4) is known to be a p-type wide bandgap material.

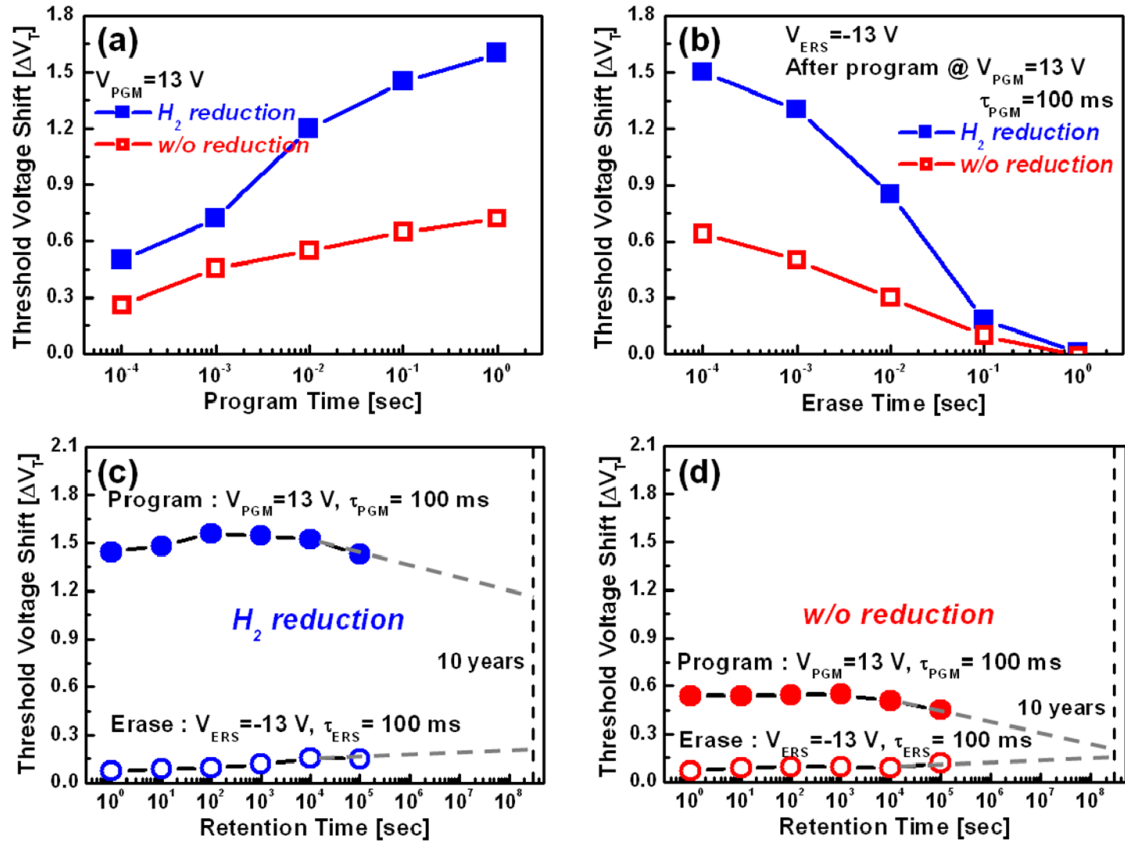


Figure 6. The electrically measured (a) program, (b) erase, and (c) retention characteristics of the reduced Co/Co-oxide composite NC embedded device, and (d) that of the oxidized one versus time variation. The leftmost inset shows the initial I - V characteristic of the device according to the drain bias of 0.05 and 1 V.

The band offset information was obtained from an earlier report [12]. The configuration of the NC storage node is based on the metallic Co core/Co-oxide shell structure for electron trap sites. When programming (see the upper row in figure 4) with gate-to-source bias, $V_{GS} = 13$ V, an electron from a channel is injected into the floating gate with the aid of a Fowler–Nordheim (FN) tunneling mechanism. The FN tunneling current density can be expressed as follows.

$$J_{\text{FN}} = K E_{\text{ox}}^2 e^{-B/E_{\text{ox}}} \quad (1)$$

$$\text{where } K = \frac{q^3 m}{8\pi h m^* \Phi_B}, \quad B = \frac{4\sqrt{2m^*} \Phi_B^2}{3\hbar q}.$$

Here, q , m , m^* , h , and Φ_B are the magnitudes of the electronic charge, electron mass, effective electron mass in silicon dioxide, Planck's constant, and potential barrier, respectively. E_{ox} , the electric field across the tunneling oxide, is the dominant parameter governing the FN tunneling current, which is inversely proportional to the thickness of the tunneling oxide. Due to the expansion of metallic core region through the hydrogen reduction process, the band bending across the tunneling oxide becomes steeper. The increasing of the electric field for the program mode causes additional FN tunneling current. Hence, the shift of the threshold voltage is enlarged at the reduced Co/Co-oxide NCs. The inset of figure 4(b) exhibits the overlapped conduction energy band diagrams of the oxidized and reduced Co/Co-oxide composite at the

tunneling oxide and it is confirmed that band bending of the reduced Co/Co-oxide is greater than that of the oxidized one.

When erasing (see the lower row in figure 4) with $V_{GS} = -13$ V, the direction of electron injection is exactly opposite to the programming case, from the floating gate to the substrate. Considering the sequential configuration of the Co-oxide shell and metallic Co core, the total tunneling probability is expressed as a multiplication form of two components; tunneling probability at the (i) Co-oxide and (ii) tunneling oxide. Considering the reduced Co/Co-oxide in figure 4(d), reduced Co/Co-oxide has a thinner quantum barrier than the oxidized Co/Co-oxide case in figure 4(c) due to reduction of the Co-oxide component, and the tunneling probability at the (i) Co-oxide is enlarged. So, the device with reduced Co/Co-oxide can have better erasing efficiency than the case of oxidized Co/Co-oxide. Regarding the tunneling probability, the inset of figure 4(d) exhibits the overlapped energy band diagrams of oxidized and reduced Co/Co-oxide composite near the tunneling oxide and the Co-oxide.

On the other hand, in the case of retention in figure 5, which is a reference point of charge preservation, a direct tunneling mechanism without external bias becomes important. Particularly, a width of potential well should be considered. In the energy band diagram with zero bias, the oxidized Co/Co-oxide composite shown in figure 5(a) has a larger portion of Co-oxide component with shallower potential

depth than the reduced Co/Co-oxide one in figure 5(b). It reveals that the charges can be tunneled out easily in the oxidized Co/Co-oxide composite device. Co-oxide, an unstable insulator, has defects induced from plasma oxidation, thereby the stored electrons at the metallic Co component can be tunneled back via these defects. Additionally, due to the increased energy spacing by the quantum confinement effect, the Fermi level of the Co component with a smaller diameter is shifted upward more than that with a larger diameter hence it reduces the band offset between the silicon substrate and the potential level of metallic Co [33]. Thereafter a large portion of the metallic Co in the reduced Co/Co-oxide composite contributes to the elongation of the retention properties.

Figure 6 shows the electrically measured program, erase, and retention characteristics according to time variation. The leftmost inset shows the initial I - V characteristic of the device. The FN tunneling mechanism was used, and a gate voltage of 13 V and -13 V with grounded source/drain was applied for the program/erase operation, respectively. As can be inferred from figure 4, the efficiency of the program/erase operation is expressed as an amount of V_T shift according to the duration of pulse time (figures 6(a) and (b)). Similarly, the data retention characteristics (figures 6(c) and (d)) are represented by the V_T drop according to time variation. That is also improved by the hydrogen annealing process in the reduced Co/Co-oxide composite NC memory device.

It should be noted that these results can provide a guideline on how to design the configuration of metal and metal oxide for memory applications. To improve the program/erase efficiency and retention properties, the portion of the metallic core should be increased via the optimization of the hydrogen annealing conditions.

4. Conclusions

In summary, the memory effects on the metallic Co core NCs surrounded by a Co-oxide shell were investigated. Through TEM images and the XPS spectrum it was confirmed that the Co-oxide was created by the oxygen plasma while the Co core was created by the hydrogen annealing process. This demonstrates the coexistence of the Co core and the Co-oxide. A suitable energy band diagram was proposed and supported by electrically measured data. The memory performance, i.e. the program, erase, and retention characteristics, can be improved by optimizing the fraction of the metallic domain through the metallic Co/Co-oxide configuration.

Acknowledgments

This research was partially supported by the NRL Program of the Korea Science and Engineering Foundation (KOSEF) grant funded by the Korean Government (MEST) (ROA-2007-000-20028-0 and ROA-2007-000-20127-0) and supported by the Nano R&D program through the National Research Foundation of Korea funded by the Ministry of Education, Science, and Technology (grant number: 2009-0082583). Also, this work was partially supported by the IT R&D

program of MKE/KEIT. (10029953, Terabit Nonvolatile Memory Development.)

References

- [1] Tiwari S, Rana F, Hanafi H, Hartstein A, Crabbe E F and Chan K 1996 *Appl. Phys. Lett.* **68** 1377
- [2] De B J 2002 *IEEE Trans. Nanotechnol.* **1** 72
- [3] Choi W K, Chim W K, Heng C L, Teo L W, Ho V, Ng V, Antoniadis D A and Fitzgerald E A 2002 *Appl. Phys. Lett.* **80** 2014
- [4] White M H, Adams D A and Bu J 2000 *IEEE Circuits Devices Mag.* **16** 22
- [5] Lee H et al 2007 *IEEE Symp. on VLSI Technology* p 144
- [6] Yater J 2009 *Int. Memory Workshop* 10–14 May
- [7] Liu Z, Lee C, Narayanan V, Pei G and Kan E C 2002 *IEEE Trans. Electron Devices* **49** 1606
- [8] Lee C, Gorur-Seetharam A and Kan E C 2003 *IEEE Int. Electron Devices Mtg* p 557
- [9] Tseng J Y, Cheng C W, Wang S Y, Wu T B, Hsieh K-Y and Liu R 2004 *Appl. Phys. Lett.* **85** 2595
- [10] Lin Y H, Chien C H, Lin C T, Chang C Y and Lei T F 2005 *IEEE Electron Device Lett.* **26** 154
- [11] Hikono T, Matsumura T, Miura A, Uraoka Y, Fuyuki T, Takeguchi M, Yoshii S and Yamashita I 2006 *Appl. Phys. Lett.* **88** 023108
- [12] Miura A, Tsukamoto R, Yoshii S, Yamashita I, Uraoka Y and Fuyuki T 2008 *Nanotechnology* **19** 255201
- [13] Shahrjerdi D, Garcia-Gutierrez D I and Banerjee S K 2007 *IEEE Electron Device Lett.* **28** 793
- [14] Black C T, Guarini K W, Ruiz R, Sikorski E M, Babich I V, Sandstrom R L and Zhang Y 2006 *IEEE Int. Electron Devices Mtg* p 1
- [15] Kästle G et al 2003 *Adv. Funct. Mater.* **13** 853
- [16] Krishnamoorthy S, Hinderling C and Heinzlmann H 2006 *Mater. Today* **9** 40
- [17] McMillan R A, Paavola C D, Howard J, Chan S L, Zaluzec N J and Trent J D 2002 *Nat. Mater.* **1** 247
- [18] Samson J, Varotto A, Nahirney P C, Toschi A, Piscopo I and Drain C M 2009 *ACS Nano* **3** 339
- [19] Le J D, Pinto Y, Seeman N C, Musier-Forsyth K, Taton T A and Kiehl R A 2004 *Nano Lett.* **4** 2343
- [20] Portney N G, Martinez-Morales A A and Ozkan M 2008 *ACS Nano* **2** 191
- [21] Claridge S A, Castleman A W, Khanna S N Jr, Murray C B, Sen A and Weiss P S 2009 *ACS Nano* **3** 244
- [22] Hwang C G 2006 *IEEE Int. Electron Devices Mtg* p 1
- [23] Ishii T, Osabe T, Mine T, Murai F and Yano K 2000 *IEEE Int. Electron Devices Mtg* p 305
- [24] Kim C-J, Ryu S-W, Choi Y-K, Chang J-J, Bae S H and Sohn B-H 2008 *Appl. Phys. Lett.* **93** 052106
- [25] Dimitrov A S and Nagayama K 1996 *Langmuir* **12** 1303
- [26] Yoon T S, Oh J, Park S H, Kim V, Jung B G, Min S H, Park J, Hyeon T and Kim K B 2004 *Adv. Funct. Mater.* **14** 1062
- [27] Förster S and Antonietti M 1998 *Adv. Mater.* **10** 195
- [28] Förster S and Plantenberg T 2002 *Angew. Chem. Int. Edn* **41** 688
- [29] Boyen H-G et al 2003 *Adv. Funct. Mater.* **13** 359
- [30] Jonsson H, Nørskov J K, Rossmeisl J, Logadottir A, Lindqvist L, Kitchin J R and Bligaard T 2004 *J. Phys. Chem. B* **108** 17886
- [31] Mattogno G, Ferragina C, Massucci M A, Patrono P and LaGinestra A 1998 *J. Electron Spectrosc. Relat. Phenom.* **46** 285
- [32] *Taurus-Medici User's Manual* 2007 (Mountain View, CA: Synopsys, Inc.)
- [33] Guan W, Long S, Liu M, Liu Q, Hu Y, Li Z and Jia R 2007 *Solid-State Electron.* **51** 806